Electronic Supplementary Material (ESI) for Dalton Transactions.

Electronic Supplementary Information (ESI)

Increase of network hydrophilicity from lvt to sql supramolecular isomers of Cu-MOFs with the bifunctional 4-(3,5-dimethyl-1*H*-pyrazol-4-yl)benzoate linker

Saskia Menzel, Simon Millan, Simon-Patrick Höfert, Alexander Nuhnen, Serkan Gökpinar, Alexa Schmitz and Christoph Janiak*

Institut für Anorganische Chemie und Strukturchemie, Heinrich-Heine-Universität Düsseldorf, Universitätsstraße 1, D-40225 Düsseldorf, Germany. *E-mail: janiak@hhu.de

Additional Emails:

Saskia.menzel@hhu.de; simon.millan@hhu.de; Hoefert@hhu.de; Alexander.Nuhnen@hhu.de; Serkan.Goekpinar@hhu.de; Alexa.Schmitz@hhu.de

IR spectra

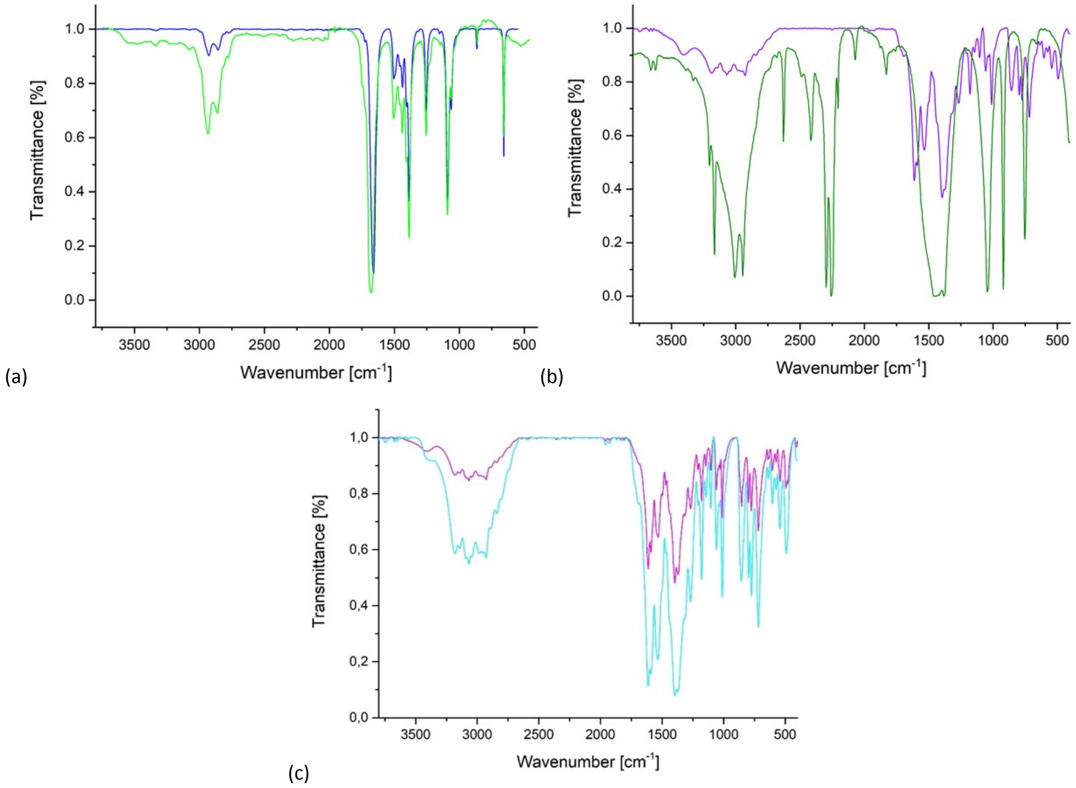

(a) (b) (c)

Fig. S0 (a) IR-Spectra (KBr) of as synthesized **sql**-[Cu(Hmpba)$_2$]·xDMF (**sql**-DMF-a.s., blue) and DMF (NIST, green);[1] (b) IR-Spectra (KBr) of as synthesized **sql**-[Cu(Hmpba$_2$]·2ACN (**sql**-ACN-a.s., violet) and ACN (NIST, dark green)[1] (c) IR-Spectra (KBr) of **sql**-DMF-act. (cyan) and of **sql**-ACN-act. (magenta). NIST: The data for the solvent IR-Spectra were download from the NIST database[1] and were plot in Origin.[2]

Powder X-ray diffractograms

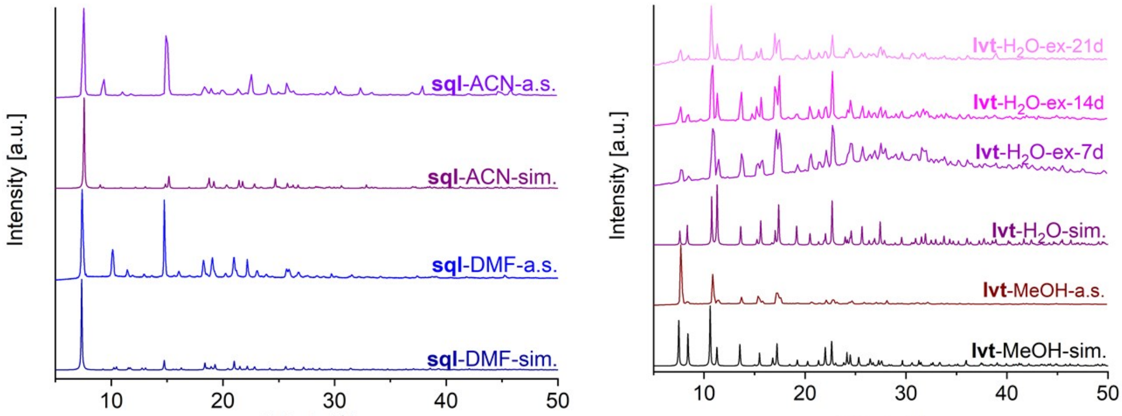

(a) (b)

Fig. S1 (a) PXRD patterns of as synthesized **sql**-DMF, **sql**-ACN and their simulations from the single-crystal structure data. (b) PXRD patterns of **lvt**-MeOH-sim., **lvt**-MeOH-a.s., **lvt**-H_2O-sim. and the different control exchange steps after 7 d, 14 d and 21 d.

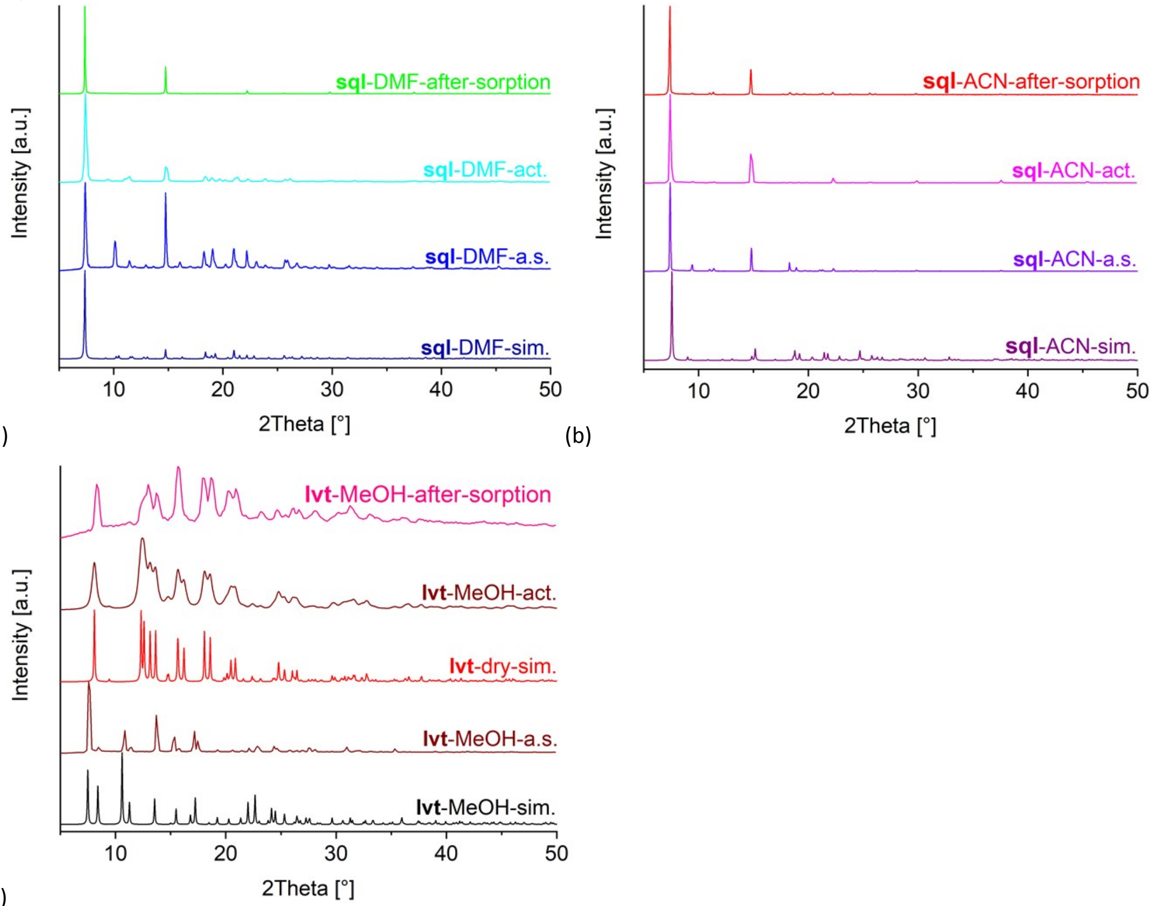

(a) (b)

(c)

Fig. S2 (a) PXRD patterns for **sql**-DMF simulated (sim.), as synthesized (a.s.), activated (act.) and after gas sorption measurements; (b) PXRD patterns for **sql**-ACN simulated, as synthesized, activated and after gas sorption measurements. (c) PXRD patterns for **lvt**-MeOH simulated, as synthesized, activated and after gas sorption measurements. The PXRD pattern of **lvt**-MeOH-act. must be matched to the PXRD pattern of **lvt**-dry-sim., which represents the air-dried sample of **lvt**-MeOH by Richardson and co-workers *(*compound 8-*dry* in ref.3*)* that still contained 1.5 water molecules.[3] Small changes between the simulated and as-synthesized patterns are due to the unavoidable solvent loss during sample preparation and measurement.

Images of the crystals

Fig. S3 Picture of the crystals of **sql**-DMF (left), **sql**-ACN (middle), **lvt**-H_2O (right).

Crystal structure information

Table S1 Crystal data and structure refinement for **sql**-DMF, **sql**-ACN and **lvt**-H_2O.

Compound	$[Cu(Hmpba)_2]\cdot xDMF$* **sql**-DMF	$[Cu(Hmpba)_2]\cdot 2ACN$ **sql**-ACN	$[Cu(Hmpba)_2]\cdot 9H_2O$ **lvt**-H_2O [d]
CCDC no.	1999766	1999767	1999768
Empirical formula	$C_{24}H_{22}CuN_4O_4\cdot 1(C_3H_7O)$	$C_{24}H_{22}CuN_4O_4\cdot 2(C_2H_3N)$	$C_{24}H_{39.94}CuN_4O_{12.96}$
M_r /g mol^{-1}	567.09	576.10	655.47
Crystal system	monoclinic	monoclinic	tetragonal
Space group	$P2_1/n$	$P2_1/c$	$I4_1/a$
a /Å	10.0436(8)	9.7946(10)	23.2432(12)
b /Å	17.2646(14)	19.5794(17)	23.2432(12)
c /Å	17.3187(14)	14.8975(14)	11.9130(7)
β /°	105.201(4)	103.587(5)	90
V /Å^3	2898.0(4)	2777.0(5)	6436.0(8)
Z	4	4	8
μ / mm^{-1}	0.80	0.83	0.75
d_{calc} /g·cm^{-3}	1.300	1.378	1.353
$F(000)$	1180	1196	2757
Crystal size /mm	0.10 × 0.05 × 0.05	0.1 × 0.06 × 0.03	0.14 × 0.12 × 0.06
T_{min}, T_{max}	0.904/1.000	0.955/1.000	0.623/0.745
No. of meas./indep./obs. refl.	39626/6386/5474	80053/10577/8382	48071/3301/3060
R_{int}	0.065	0.029	0.123
$(\sin \theta/\lambda)_{max}$ /Å^{-1}	0.641	0.796	0.627
R $[F^2>2\sigma(F^2)]/wR(F^2)$ [a]	0.0909/0.2338	0.035/0.1022	0.0395/0.1088
R_1/wR_2 (all data) [a]	0.1003/0.2380	0.0485/0.1113	0.0420/0.1103
Goodness-of-fit on F^2 [b]	1.181	1.034	1.138
No. of reflections	6386	10577	3301
No. of parameters	355	367	236
No. of restrains	0	6	15
$\Delta\rho_{max}$, $\Delta\rho_{min}$ [c] /e Å^{-3}	2.10, –1.15	0.67, –0.40	0.71, –0.48

* x=1DMF found and refined, 0.5DMF squeezed; [a] $R_1 = [\sum(||F_o| - |F_c||)/\sum|F_o|]$; $wR_2 = [\sum[w(F_o^2 - F_c^2)^2]/\sum[w(F_o^2)^2]]^{1/2}$.

[b] Goodness-of-fit = $[\sum[w(F_o^2 - F_c^2)^2]/(n - p)]^{1/2}$. [c] Largest difference peak and hole.

[d] Cell constants for comparison for **lvt**-MeOH: a = 23.5927(4) Å, b = 23.5927(4) Å, c = 11.7356(3) Å.

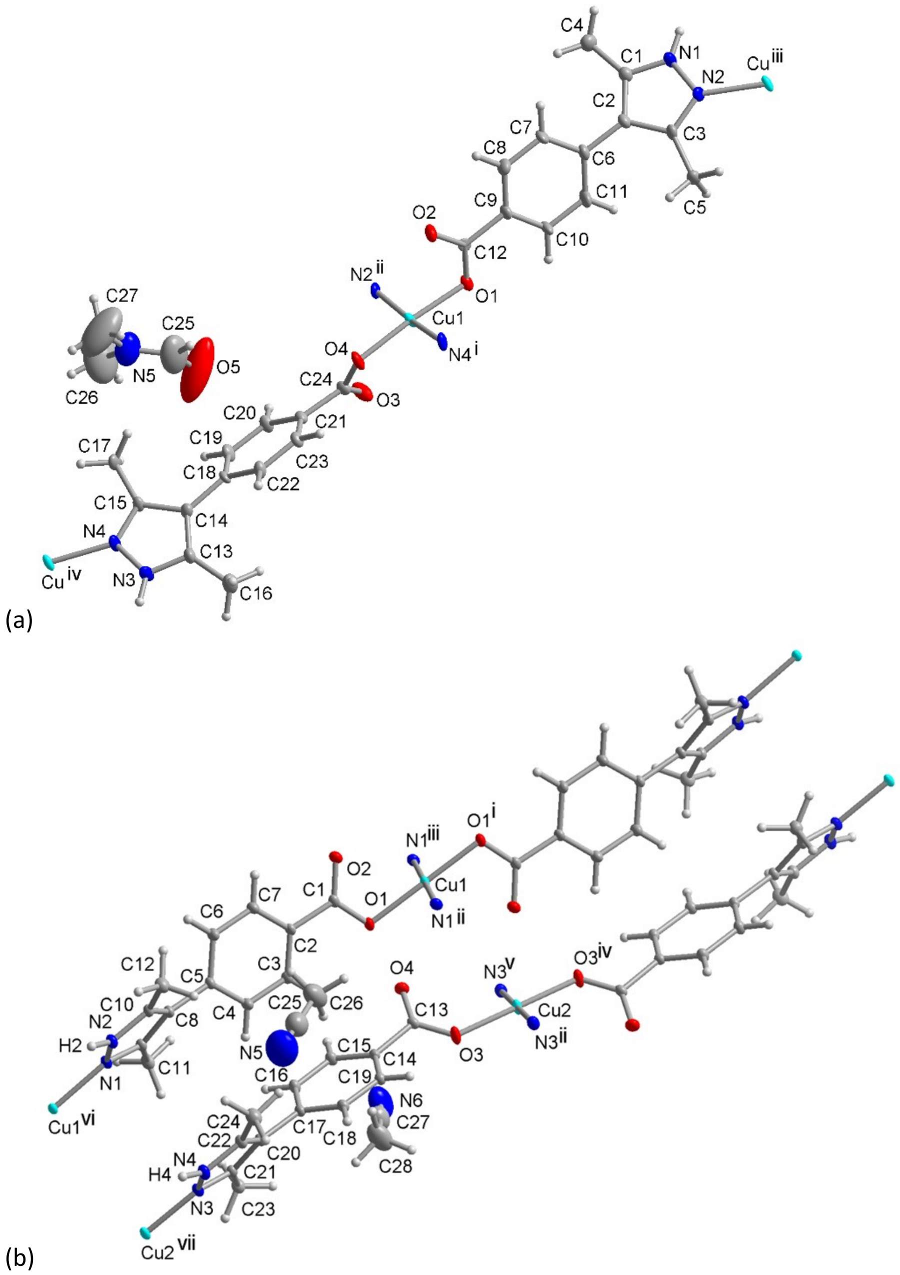

Fig. S4 (a) Metal-ligand coordination in [Cu(Hmpba)$_2$]·xDMF (**sql**-DMF) (70% thermal ellipsoids) with full atom numbering scheme and the located DMF solvent molecule. Disordered solvent molecules resulting in non-refinable electron density were removed via the SQUEEZE command in PLATON.[4] Symmetry transformations: i = x+1/2, -y+3/2, z+1/2; ii = x-1/2, -y+1/2, z-1/2; iii= x+1/2, -y+1/2, z+1/2; iv= x-1/2, -y+3/2, z-1/2. (b) Extended asymmetric unit of [Cu(Hmpba)$_2$]·2ACN (**sql**-ACN) with two symmetry-independent formula units (50% thermal ellipsoids). Symmetry transformations: i = -*x*+1, -*y*+1, -*z*+1; ii = *x*, -*y*+3/2, *z*-1/2; iii = -*x*+1, *y*-1/2, -*z*+3/2; iv = -*x*+2, -*y*+1, -*z*+1; v = -*x*+2, *y*-1/2, -*z*+3/2; vi = -*x*+1, *y*+1/2, -*z*+3/2; vii = -*x*+2, *y*+1/2, -*z*+3/2.

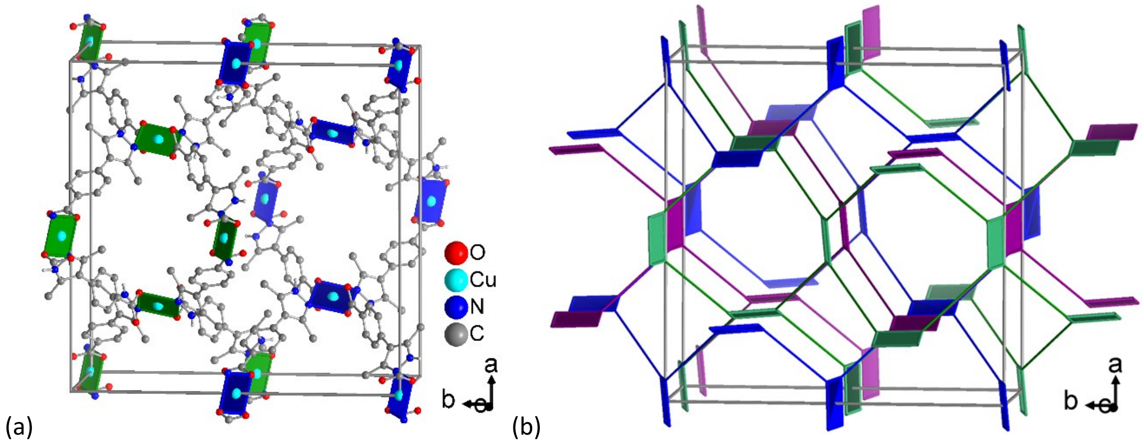

Fig. S5 (a) Section of two of the interpenetrating **lvt** nets of the structure [Cu(Hmpba)$_2$]·9H$_2$O, **lvt**-H$_2$O with indication of the square-planar Cu coordination sphere. (b) Schematic presentation of the three interpenetrating **lvt**-nets. In the **lvt**-network (Schäfli symbol $4^2.8^4$), the Cu atoms, which each connect to four ligands, can be described as 4-connecting nodes (square 4-c {CuN$_2$O$_2$}-Cluster). The Schäfli symbol indicates that the network contains 4- and 8-membered rings. The 8-membered rings span an oval pore along the ac plane (not shown). The interpenetration type is Ia, which means that the networks are connected via a single translation. The interpenetrating vectors are as follows: [3/2,3/2,3/2][0,1,0][1,0,0].

Table S2 Selected bond lengths (Å) and angles (°) for **sql**-DMF, **sql**-ACN and **lvt**-H$_2$O.

Bond lengths (Å)		**Angles (°)**	
sql-DMF			
Cu1- O3	1.949(4)	O3—Cu1—O1	175.74(19)
Cu1- O1	1.970(4)	O3—Cu1—N4^{i}	88.73(19)
Cu1- N4^{i}	1.980(5)	O1—Cu1—N4^{i}	88.82(18)
Cu1- N2^{ii}	1.986(5)	O3—Cu1—N2^{ii}	91.84(19)
		O1—Cu1—N2^{ii}	91.10(18)
		N4^{i}—Cu1—N2^{ii}	171.6(2)
Symmetry transformations: i = x+1/2, -y+3/2, z+1/2; ii = x-1/2, -y+1/2, z-1/2			
sql-ACN			
Cu1- O1	1.9532(8)	O1—Cu1—O1^{i}	180.0
Cu1- O1^{i}	1.9533(8)	O1—Cu1—N1^{ii}	90.44(4)
Cu1- N1^{ii}	1.9985(10)	O1^{i}—Cu1—N1^{ii}	89.57(4)
Cu1- N1^{iii}	1.9985(9)	O1—Cu1—N1^{iii}	89.56(4)
		O1^{i}—Cu1—N1^{iii}	90.43(4)
		N1^{ii}—Cu1—N1^{iii}	180.0
Cu2- O3^{iv}	1.9369(8)	O3^{iv}—Cu2—O3	180.0
Cu2- O3	1.9370(8)	O3^{iv}— Cu2—N3^{ii}	94.55(4)
Cu2- N3^{ii}	1.9610(10)	O3— Cu2—N3^{ii}	85.45(4)
Cu2- N3^{v}	1.9610(10)	O3^{iv} — Cu2—N3^{v}	85.45(4)
		O3 — Cu2—N3^{v}	94.55(4)
		N3^{ii}—Cu2—N3^{v}	180.0

Symmetry transformations: i= -*x*+1, -*y*+1, -*z*+1; ii= *x*, -*y*+3/2, *z*-1/2; iii= -*x*+1, *y*-1/2, -*z*+3/2; iv= -*x*+2, -*y*+1, -*z*+1.			
lvt-H_2O			
Cu1—O1^{i}	1.9446 (14)	O1^{i}—Cu1—O1^{ii}	180.00 (8)
Cu1—O1^{ii}	1.9446 (14)	O1^{i}—Cu1—N2^{iii}	88.45 (7)
Cu1—N2^{iii}	1.9849 (17)	O1^{ii}—Cu1—N2^{iii}	91.55 (7)
Cu1—N2	1.9850 (17)	O1^{i}—Cu1—N2	91.55 (7)
		O1^{ii}—Cu1—N2	88.45 (7)
		N2^{iii}—Cu1—N2	180.0
Symmetry transformations: i= y-3/4, -x+3/4, -z+3/4; ii= -y+3/4, x+1/4, z-3/4; iii= -x, -y+1, -z.			

Non-covalent interactions

PLATON was used for the investigation of the supramolecular interactions listed in Table S3.

Despite the presence of phenyl- and azole-π-systems, there are no π---π interactions. The structures feature rather long ring centroid-centroid distances (>4.0 Å) together with non-parallel ring planes (α >> 0°) and large slip angles (β, γ > 30°). In comparison, significant π-stacking shows rather short centroid-centroid contacts (<3.8 Å), near parallel ring planes (α < 10° to ~0° or even exactly 0° by symmetry), small slip angles (β, γ 25°) and vertical displacements (slippage <1.5 Å) which translate into a sizable overlap of the aryl-plane areas.[5] Significant intermolecular C-H···π contacts start below around 2.7 Å for the (C-)H···ring centroid distances with H-perp also starting at below 2.6-2.7 Å and C-H··Cg > 145° (Scheme S1).[6]

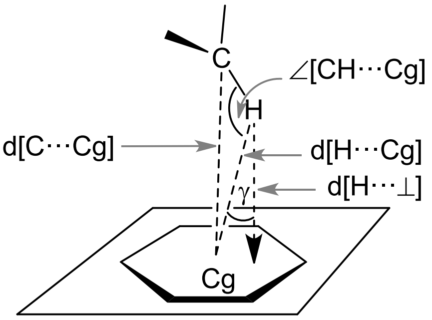

Scheme S1 Graphical presentation of the parameters used for the description of CH-π interactions.

Table S3 Interlayer CH-π and N-H···O hydrogen bonding interactions in **sql**-DMF, **sql**-ACN and **lvt**-H_2O.

	CH··π	**H···Cg1 / Å**	**H···⊥ / Å**	**γ/°**	**C-H···Cg1 /°**	**C···Cg1 / Å**	**C-H, Cg1 /°**
sql-DMF	C(7)-H(7) ··Cg1^{vii}	2.85	2.81	9.62	145	3.67	62
	C(10)-H(10) ··Cg1^{viii}	2.89	2.77	16.7	157	3.78	61
sql-ACN	C(3)-H(3) ··Cg1	2.81	2.76	11.1	139	3.58	59
	C(6)-H(6) ··Cg1^{iii}	2.85	2.84	5.61	146	3.68	59
lvt-H_2O	C(11)-H(11)·Cg1	3.00	2.91	13.6	147	3.83	53

	D-H··A	**D-H/Å**	**H··A /Å**	**D··A /Å**	**D-H··A /°**
sql-DMF	N(1)-H(1) ··O2^{v}	0.95(8)	1.77(8)	2.700(7)	165(7)
	N(3)-H(3) ··O4^{vi}	0.82(9)	1.94(8)	2.653(7)	145(8)
sql-ACN	N(2)-H(2) ··O4^{vi}	0.87(2)	1.85(2)	2.6791(14)	158(2)
	N(4)-H(4) ··O2^{vi}	0.83(2)	1.99(2)	2.7459(13)	150(2)
lvt-H_2O	N1—H1···O1^{ii}	0.85(3)	2.41(3)	2.831(2)	111(2)
	N1—H1···O3^{v}	0.85(3)	2.03(3)	2.811(3)	153(3)
	O3—H3B···O2^{i}	0.82(1)	1.94(1)	2.758(3)	178(4)
	O6—H6B···O2^{i}	0.82(1)	2.01(1)	2.814(3)	169(5)
	O7—H7A···O7^{vi}	0.82(1)	2.09(2)	2.897(8)	168(8)
	O4—H4B···O4^{vii}	0.81(1)	2.05(2)	2.784(4)	150(4)

Symmetry transformations: **sql**-DMF: v = -*x*+3/2, *y*-1/2, -*z*+3/2; vi = -*x*-1/2, *y*+1/2, -*z*+1/2; vii =1-x, 1-y, 1-z; viii = -x, 1-y, 1-z , **sql**-ACN: iii = -*x*+1, *y*-1/2, -*z*+3/2; vi = -*x*+1, *y*+1/2, -*z*+3/2; **lvt**-H_2O i= *y*-3/4, -*x*+3/4, -*z*+3/4; ii= -*y*+3/4, *x*+1/4, *z*-3/4; v= *y*-1/4, -*x*+1/4, -*z*+1/4; vi= -*x*+1, -*y*+1, -*z*; vii= -*x*, -*y*+1/2, *z*. **Cg1** refers to the ring centre of gravity in the ring C18-C19-C20-C21-C22-C23 for **sql**-DMF; C14-C15-C16-C17-C18-C19 for **sql**-ACN and C6-C7-C8-C9-C10-C11 for **lvt**-H_2O. **H···⊥:** Perpendicular distance of H to ring plane; **γ:** Angle between Cg-H vector and ring J normal; **C-H···Cg1:** C-H-Cg Angle**;** **C··Cg1:** Distance of C to Cg (see also Scheme S1); **C-H, Cg1:** Angle of the X-H bond with the π -plane (i.e.' Perpendicular = 90 degrees, Parallel = 0 degrees).

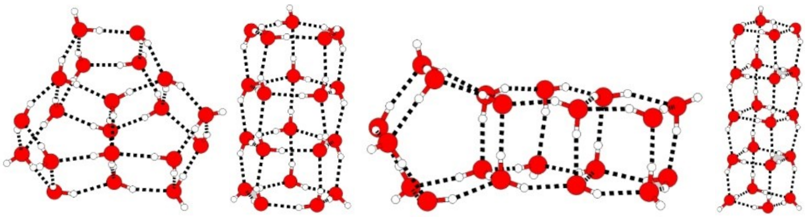

Fig. S6 Low-energy isomers for $(H_2O)_{20}$-clusters based on 4- to 6-membered ring structures (Figure taken from L. Xu et al.).[7]

Thermogravimetric analysis, TGA

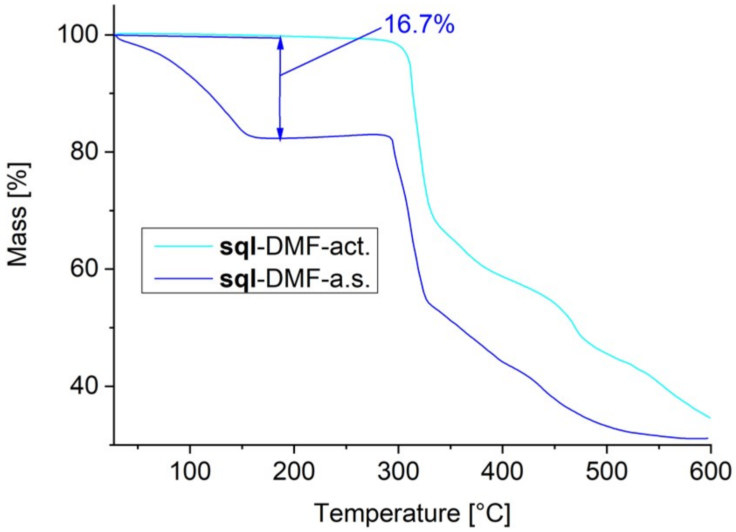

Fig. S7 TGA curves of the as-synthesized (a.s.) and activated (act.) materials for **sql**-$[Cu(Hmpba)_2]\cdot xDMF$, **sql**-DMF in the temperature range 25-600 °C with a heating rate of 5 K min^{-1} under nitrogen atmosphere. The loss of 16.7% corresponds to 1-1.5 DMF molecules calc. 12.84% for 1 DMF and 18.10% for 1.5 DMF. Deviations in the found and calculated mass percent for the solvent loss based on the single-crystal X-ray structure results are due to the already occurring solvent loss during sample preparation (drying and weighing) before the TGA measurement. The small mass increase by **sql**-DMF-a.s. is due to balance fluctuation.

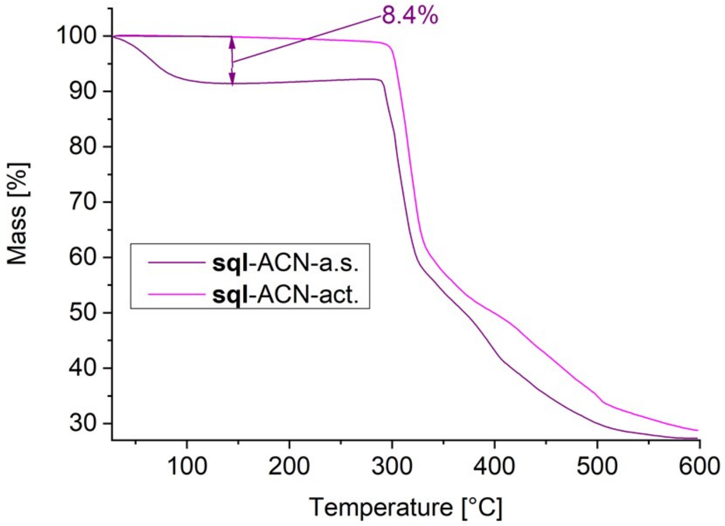

Fig. S8 TGA curves of the as-synthesized (a.s.) and activated (act.) materials for **sql**-$[Cu(Hmpba)_2]\cdot 2ACN$, **sql**-ACN in the temperature range 25-600 °C with a heating rate of 5 K min^{-1} under nitrogen atmosphere. The loss of 8.4% corresponds to 1.1 ACN molecules; calc. 7.64% for 1 ACN and 14.20% for 2 ACN molecules. Deviations in the found and calculated mass percent for the solvent loss based on the single-crystal X-ray structure results are due to the already occurring solvent loss during sample preparation (drying and weighing) before the TGA measurement. The small mass increase by **sql**-ACN-a.s. is solely due to balance fluctuation. $[Cu(Hmpba)_2]\cdot 1ACN$: $C_{26}H_{25}CuN_5O_5$, 535.06 g/mol; $[Cu(Hmpba)_2]\cdot 1.5ACN$: $C_{26.3}H_{25.45}CuN_{5.15}O_4$, 555.58 g/mol.

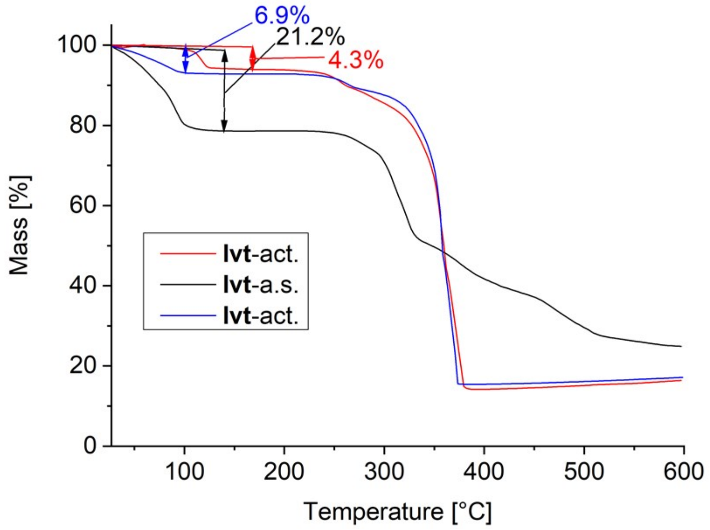

Fig. S9 TGA curves of the as-synthesized (a.s.) and activated (act.) materials for **lvt**-[Cu(Hmpba)$_2$]·4MeOH·1H$_2$O, **lvt**-MeOH (red curve: activated overnight at 160 °C; blue curve: activated at 160 °C for 8 h) in the temperature range 25-600 °C with a heating rate of 5 K min^{-1} under nitrogen atmosphere. The loss of 21.2% corresponds to 4 MeOH and 0.5/1H$_2$O; calc. 21.5/22.0%, 4.3% corresponds to 1.5 H$_2$O and 6.9% corresponds to 2 H$_2$O, which have been adsorbed by the activated compound upon handling. It has been authenticated by Richardson and co-workers with single-crystal X-ray diffraction (compound 8-dry in his publication) that compound **lvt**-MeOH-act. still contained 1.5 water molecules.[3]

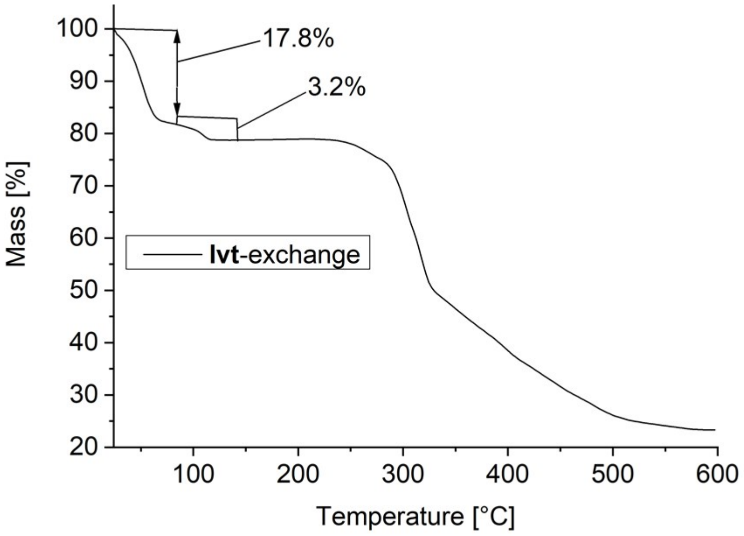

Fig. S10 TGA curves of the solvent-exchanged compound **lvt**-[Cu(Hmpba)$_2$] ·9H$_2$O, **lvt**-H$_2$O in the temperature range 25-600 °C with a heating rate of 5 K min^{-1} under nitrogen atmosphere. The loss of 17.8% corresponds to ~6.5 H$_2$O, the additional 3.2% corresponds to ~1 H$_2$O. Together, the loss of 21.0% matches the loss of 7.5 H$_2$O (calc. 20.6%). Deviations in the found and calculated mass percent for the solvent loss based on the single-crystal X-ray structure results are due to the already occurring solvent loss during sample preparation (drying and weighing) before the TGA measurement. As for **lvt**-MeOH, it can be assumed that 1.5 water molecules are still retained in the activated structure up to 250 °C. The digestion NMR of **lvt**-H$_2$O verifies the absence of MeOH.
[Cu(Hmpba)$_2$]·9H$_2$O: $C_{24}H_{40}CuN_4O_{13}$, 656.15 g/mol.

Characterization of the solvent exchange via ^{1}H-NMR studies

For the ^{1}H-NMR experiments 10 mg of the MOF sample were suspended in 0.7 mL DMSO-d_6 and digested by the addition of 20 µL of DCl (37% in D_2O). Complete exchange of MeOH against H_2O in **lvt**-MeOH can be assumed from the absence of the MeOH methyl group (at 3.10 ppm) (Figure S12). The signals around 6.73/6.78 ppm are from protonated water ($H_2O+H_3O^+$).

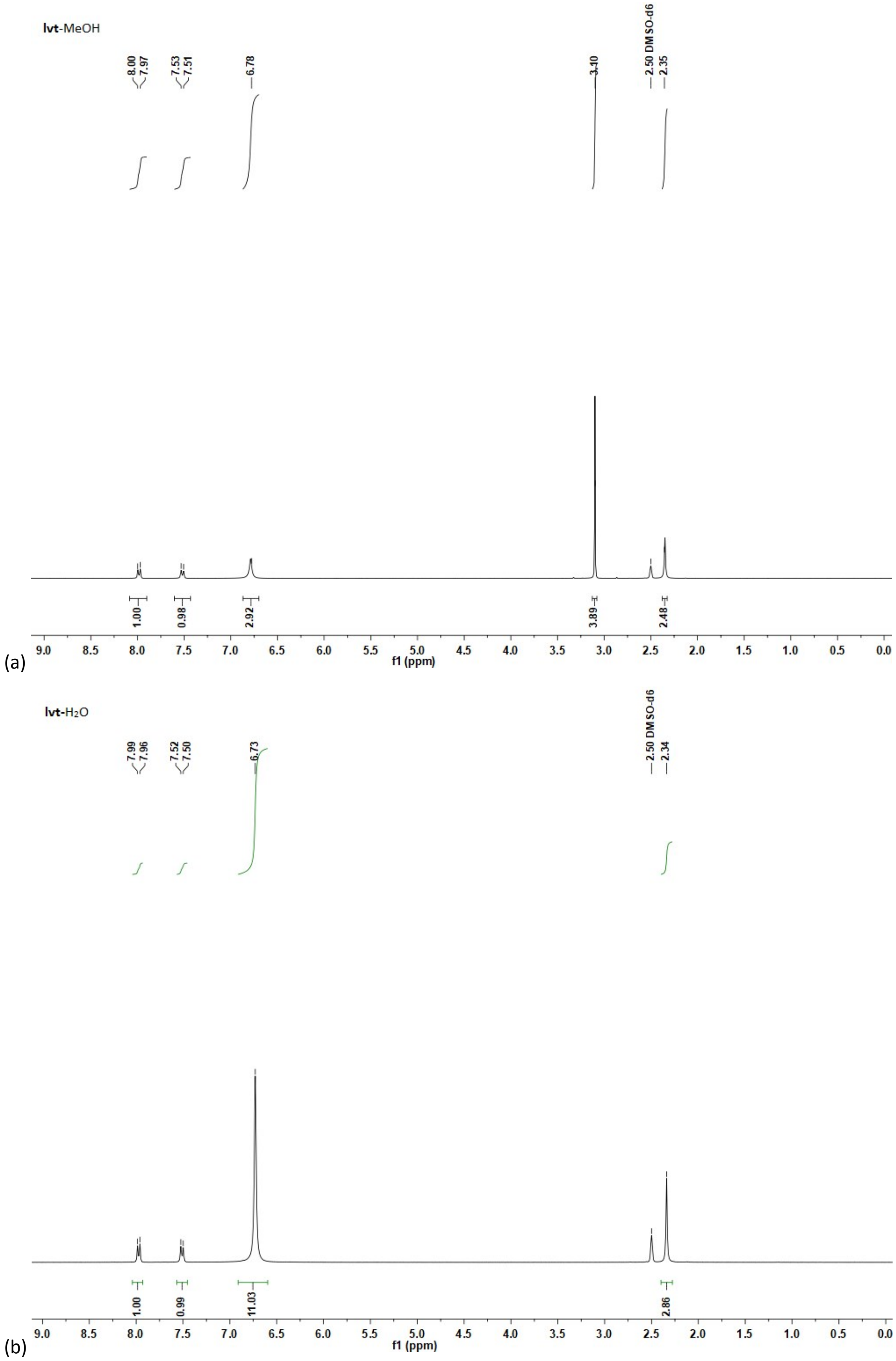

Fig. S11 ^{1}H-NMR digestion spectrum of (a) **lvt**-MeOH and (b) **lvt**-H_2O in DMSO-d_6 and DCl.

Gas sorption measurements

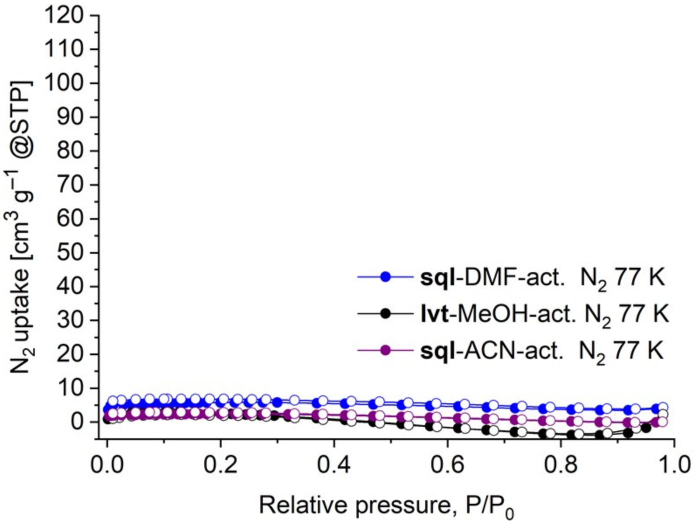

Fig. S12 N_2 Sorption isotherms for **sql**-DMF-act., **sql**-ACN-act. and **lvt**-MeOH-act. with the adsorption points as filled symbols and the desorption points as open symbols.

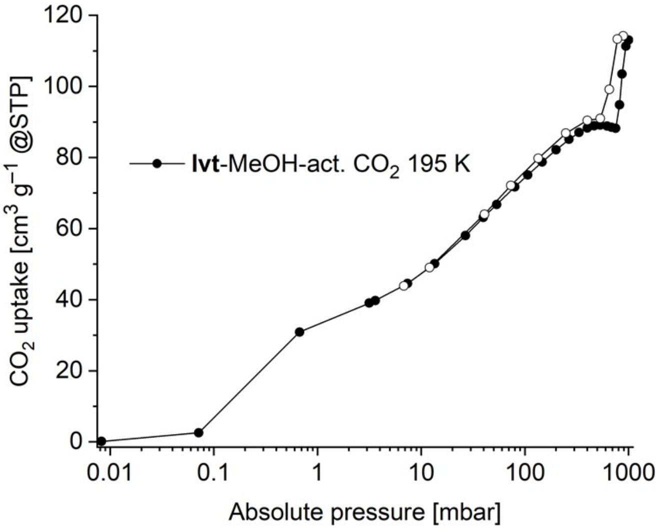

Fig. S13 CO_2 Sorption isotherm for **lvt**-MeOH-act. at 195 K with the adsorption points as filled symbols and the desorption points as open symbols.

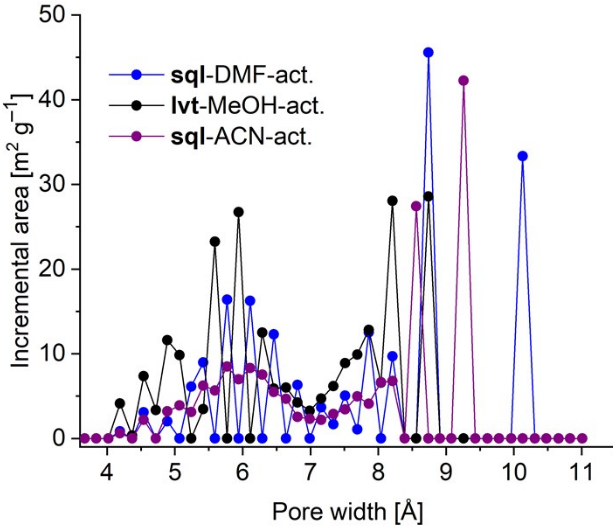

Fig. S14 NLDFT pore size distribution curves for **sql**-DMF-act., **sql**-ACN-act. and **lvt**-MeOH-act. from CO_2 adsorption isotherms (at 273 K, Fig. S16a). Note that the charts reflect a relatively crude DFT-based estimation and the jagged lines are caused by large quantization steps. The pore size distribution was estimated using nonlocal density functional theory (NLDFT) with a "slit-pore model".

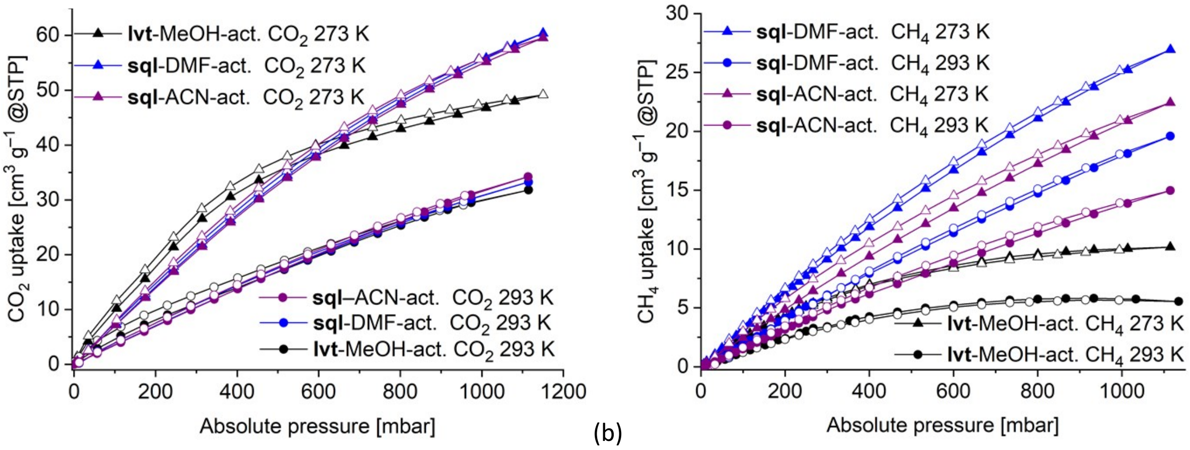

(a) (b)

Fig. S15 (a) CO_2 Sorption isotherms of **lvt**-MeOH-act., **sql**-DMF-act. and **sql**-ACN-act. at 293 K and 273 K with the adsorption points as filled symbols and the desorption points as open symbols (b) CH_4 Sorption isotherms of **lvt**-MeOH-act., **sql**-DMF-act. and **sql**-ACN-act. at 293 K and 273 K with the adsorption points as filled symbols and the desorption points as open symbols.

Calculated pore volumes and experimental gas uptake

The theoretical surface area and pore volume of the 2D frameworks [Cu(Hmpba)$_2$]·xDMF (**sql**-DMF), [Cu(Hmpba)$_2$]·2ACN (**sql**-ACN) and [Cu(Hmpba)$_2$]·4MeOH·1H_2O (**lvt**-MeOH) were calculated with the program by a 'Void' calculation with Mercury[8] and by a 'Calc Void/Solv' calculation with PLATON.[4] The calculated values are listed in Table S4.

Table S4 Calculated surface areas and pore volumes.

	sql-DMF	**sql**-ACN	**lvt**-MeOH	**lvt**-H_2O (water completely deleted)	**lvt**-H_2O (O_3 left only)
Z; $M_{\text{asym unit}}$ [g mol^{-1}]; V from X-ray structures; cf. Table S1, ESI	4; 494; 2898	4; 494; 2777	8; 494 6532	8; 494 6436	8; 534 6436
Mercury 'Void' calculation [a]					
(probe radius 1.2 Å, grid spacing 0.7 Å)	calc. using solvent accessible surface				
void volume, $V_{\text{unit cell}}$ [Å^3] (% of unit cell volume) - specific [cm^3 g^{-1}] [a]	333 (11.5) 0.10	232 (8.30) 0.07	418 (6.40) 0.06	784 (12.2) 0.12	505 (7.80) 0.07
	calc. using contact surface				
void volume, $V_{\text{unit cell}}$ [Å^3] (% of unit cell volume) - specific [cm^3 g^{-1}] [a]	870 (30.0) 0.26	742 (26.7) 0.23	1693 (25.9) 0.25	2293 (35.6) 0.34	1809 (28.1) 0.26
Platon 'Calc Void/Solv' calculation [b]					
tot. pot. solv. area volume (SAV) [Å^3] (% of unit cell vol.) - specific pore volume [cm^3 g^{-1}] from SAV[a]	928 (32.0) 0.28	859 (30.9) 0.26	2164 (33.1) 0.33	2515 (39.1) 0.38	2029 (31.5) 0.29
results from experimental CO_2 sorption data [c]					
$V_{\text{micro}}(CO_2)$ [c] [cm^3 g^{-1}] at 195 K at 1.0 bar	0.20	0.23	at 0.75 bar 0.16 at 1.0 bar 0.21		
experimental gas uptake					
CO_2 [mmol·g^{-1}] (195 K, 1.0 bar)	4.90	4.00	at 0.75 bar 3.90 at 1.0 bar 5.00		
- x 44 g/mol = CO_2 [g g^{-1}]	0.22	0.18	at 0.75 bar 0.15 at 1.0 bar 0.22		
-- / ρ_{CO2} [d] = CO_2 [cm^3 liq. CO_2/g MOF]	0.20	0.16	at 0.75 bar 0.14 at 1.0 bar 0.20		
pore filling CO_2 [cm^3 liq. CO_2/g MOF] / specific pore volume [cm^3 g^{-1}] from SAV x 100%	71	76	at 0.75 bar 42 at 1.0 bar 61		
CO_2 [mmol·g^{-1}] (298 K, 20 bar)	3.5	3.3	2.8		
- x 44 g/mol = CO_2 [g g^{-1}]	0.15	0.14	0.12		
-- / ρ_{CO2} [d] = CO_2 [cm^3 liq. CO_2/g MOF]	0.22	0.20	0.17		
pore filling CO_2 [cm^3 liq. CO_2/g MOF] / specific pore volume [cm^3 g^{-1}] from SAV x 100%	79	95	52		

[a] Probe radius 1.2 Å, grid spacing 0.7 Å; values calculated using 'contact surface'. Mercury CSD 3.9, Program for Crystal Structure Visualisation, Exploration and Analysis from the Cambridge Crystallographic Data Center, Copyright CCDC 2001-2016, http://www.ccdc.cam.ac.uk/mercury/

[b] Specific surface area calculated according to ($S_{\text{unit cell}} \times N_A$)/(Z × $M_{\text{asym unit}}$); specific pore volume calculated according to ($V_{\text{unit cell}} \times N_A$)/(Z × $M_{\text{asym unit}}$) or (SAV × N_A)/(Z × $M_{\text{asym unit}}$); N_A = Avogadro's constant: $6.022 \cdot 10^{23}$ mol^{-1}, Z = number of

asymmetric formula units, $M_{\text{asym unit}}$ = molecular weight of asymmetric formula unit [in g mol^{-1}]. As a help to reproduce the specific number the values for Z and $M_{\text{asym unit}}$ from the X-ray structures are included.

[c] Measurements on an ASAP 2020 automatic sorption analyzer (Micromeritics).

[d] density of 1.08 g cm^{-3} of liquid CO_2 at 195 K to approximate the volume of CO_2 adsorbed in the MOFs at 1.0 bar and density of 0.712 g cm^{-3} of liquid CO_2 at 298 K to approximate the volume of CO_2 adsorbed in the MOFs at 20.0 bar.

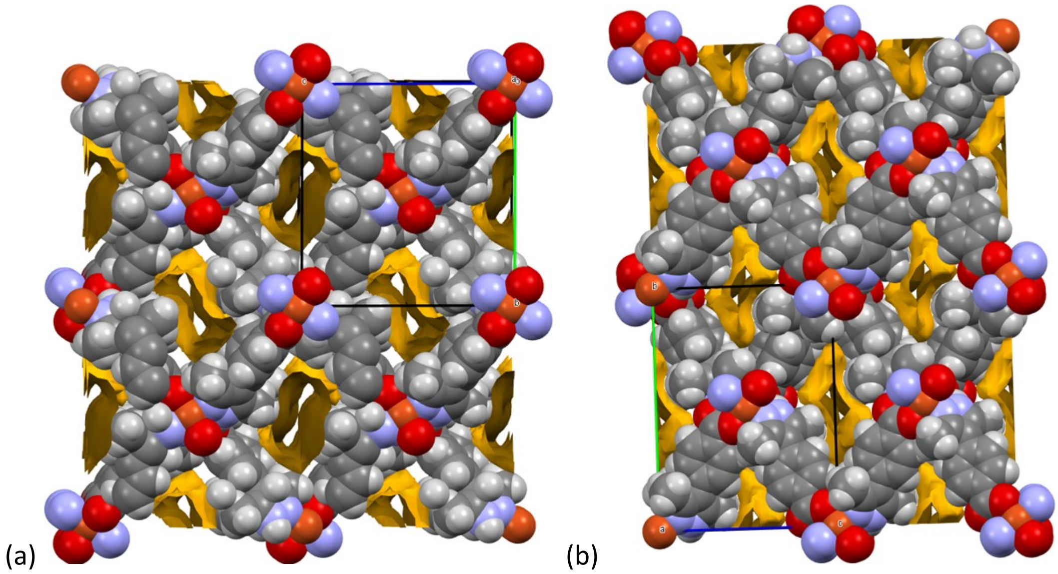

Fig S16 Solvent accessible surface (dark brown) using a probe radius of 1.2 Å for the cavities in (a) **sql**-DMF along the *a* direction, (b) **sql**-ACN along the *a* direction (the two images are not drawn to scale) from a 'void calculation' with the program Mercury (Mercury CSD 3.9, Program for Crystal Structure Visualisation, Exploration and Analysis from the Cambridge Crystallographic Data Center, Copyright CCDC 2001-2016, http://www.ccdc.cam.ac.uk/mercury/).

Heat of adsorption calculation

For the virial fit the three isotherms measured at two different temperatures are brought into an ln*p* vs. *n* form (Fig. S17). The following equation is then used to fit all three isotherms simultaneously, that is with the same fitting parameters *a_i* and *b_i*.

$$\ln p = \ln n + \frac{1}{T}\sum_{i=0}^{m} a_i n^i + \sum_{i=0}^{m} b_i n^i$$

In the equation, p is the pressure in kPa, n is the of total amount adsorbed in mmol/g, T is the temperature in K (e.g 273 K, 293 K), a_i and b_i are the virial coefficients and m represents the number of coefficients required to adequately fit the isotherms.

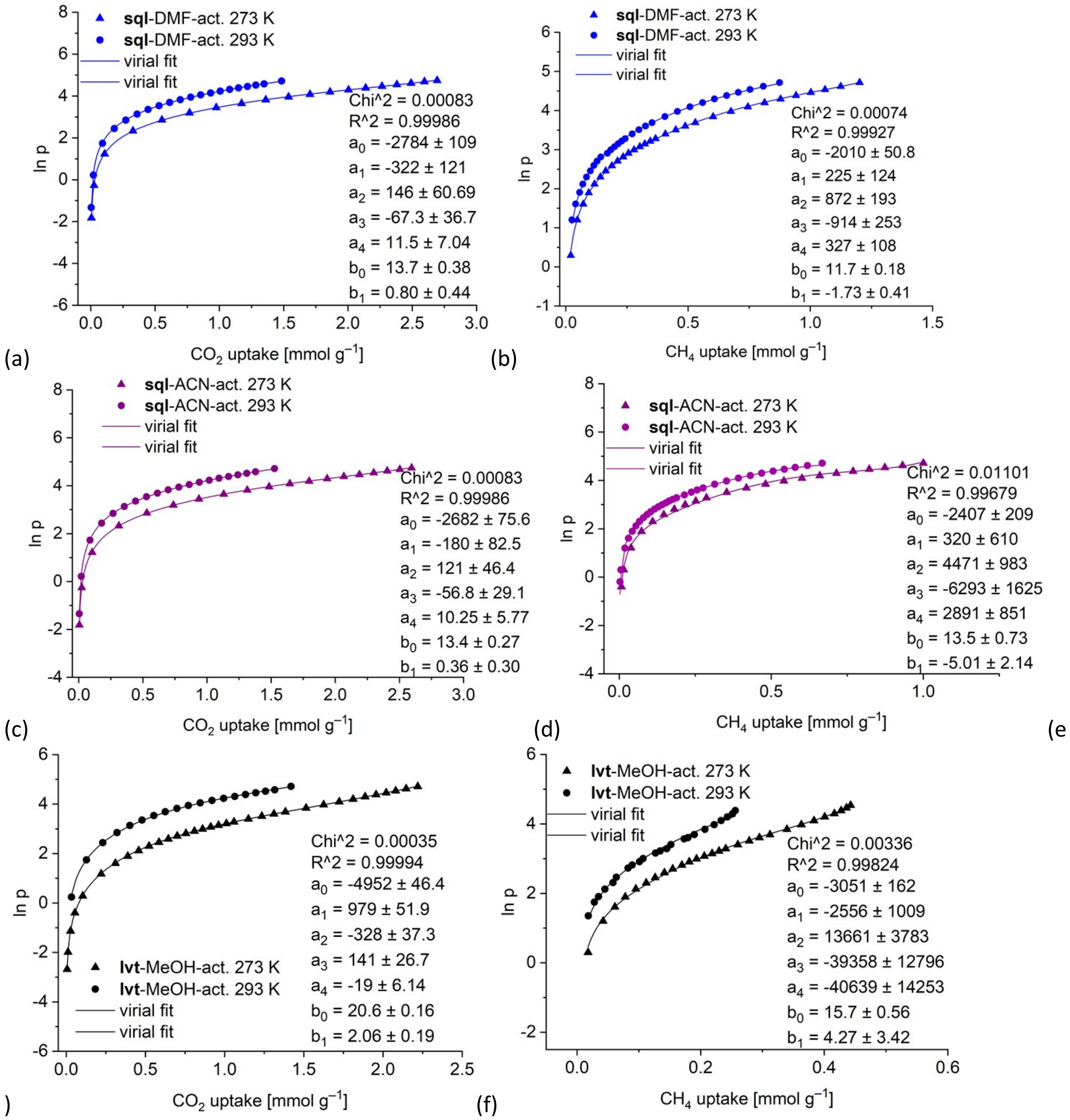

Fig S17 Virial analysis for CO_2 (a, c, e) and CH_4 (b, d, f) adsorption isotherms of **sql**-DMC-act. (a, b), **sql**-ACN-act. (c, d) and **lvt**-MeOH-act. (e, f) at 273 K and 293 K with the fitting parameters (virial coefficients) a_i and b_i.

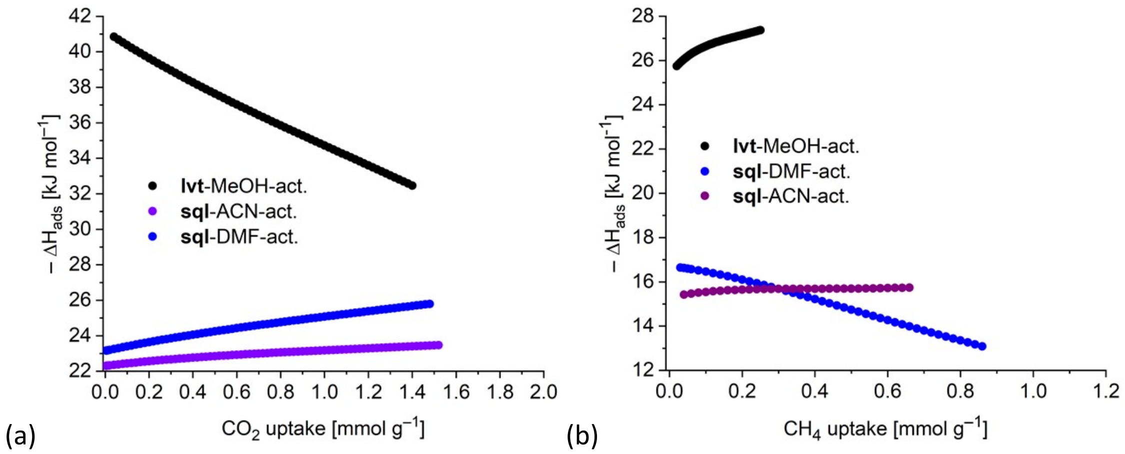

Fig S18 Isosteric enthalpy of adsorption of CO_2 (a) and CH_4 (b) for **sql**-DMF-act., **sql**-ACN-act. and **lvt**-MeOH-act. from the respective isotherms at 273 K and 293 K (cf. Fig. S16). The increase of ΔH_{ads} for CH_4 in **lvt**-MeOH can be attributed to the less steep CH_4 uptake of the 293 K versus the 273 K isotherm (Fig. S16b).

Table S5 Overview of the results from the Henry-Plots.

Compound	**Temp. [K]**	**Gradient CO_2 [cm^3/g]**	**Gradient CH_4 [cm^3/g]**	**Selectivity CO_2: CH_4**
lvt-MeOH-act.	273	0.118	0.025	4.4:1
lvt-MeOH-act.	293	0.035	0.012	2.9:1
sql-DMF-act.	273	0.068	0.032	2.1:1
sql-DMF-act.	293	0.034	0.020	1.7:1
sql-ACN-act.	273	0.069	0.024	2.8:1
sql-ACN-act.	293	0.034	0.016	2.1:1

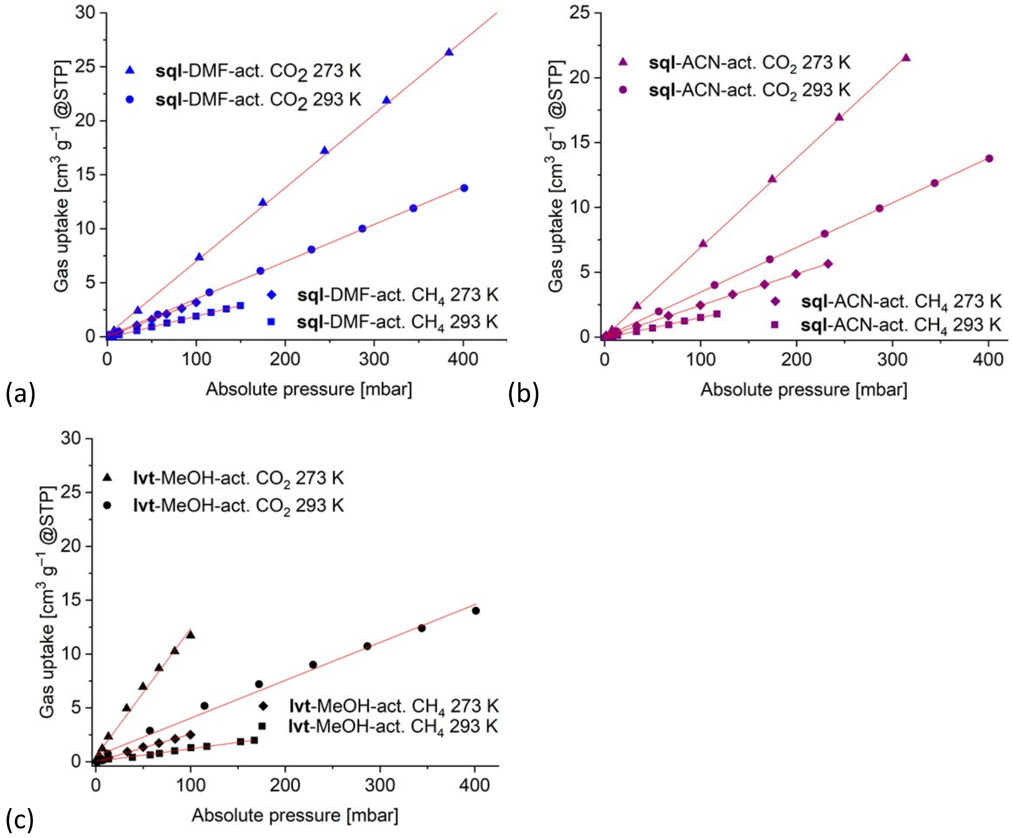

Fig. S19 Henry-Plots for CO_2 and CH_4 from the adsorption isotherms at 273 K and 293 K for (a) **sql**-DMF-act., (b) **sql**-ACN-act. and (c) **lvt**-MeOH-act.; the regression lines are in red color.

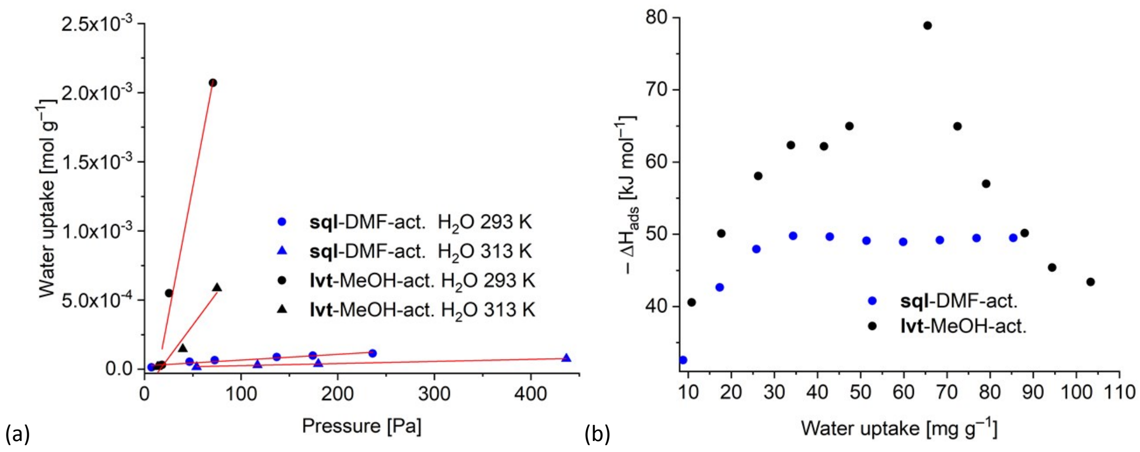

Fig. S20 (a) Henry-Plot from water adsorption isotherm at 293 K and at 313 K for **sql**-DMF-act. and **lvt**-MeOH-act.; the regression lines are in red color. (b) Isosteric enthalpy of adsorption for water adsorption at **sql**-DMF-act. and **lvt**-MeOH-act. Error margins for ΔH_{ads} can be ±10 kJ/mol.[9,10] Consequently too small deviations for ΔH_{ads} values should not overemphasized. The calculated increase for ΔH_{ads} in the range of 54-70 mg/g H_2O uptake was confirmed by repeated isotherm measurements and can be due to an exothermic process such as the rearrangement of already adsorbed H_2O molecules towards a closer, energetically more favorable configuration.

Table S6 Overview of the Henry constants from water sorption isotherms.

Compound	Temp. [K]	Henry-constant [g/mol·Pa]
lvt-MeOH-act.	293	$3.7 \cdot 10^{-5}$
lvt-MeOH-act.	313	$9.4 \cdot 10^{-6}$
sql-DMF-act.	313	$1.5 \cdot 10^{-7}$
sql-DMF-act.	293	$4.1 \cdot 10^{-7}$

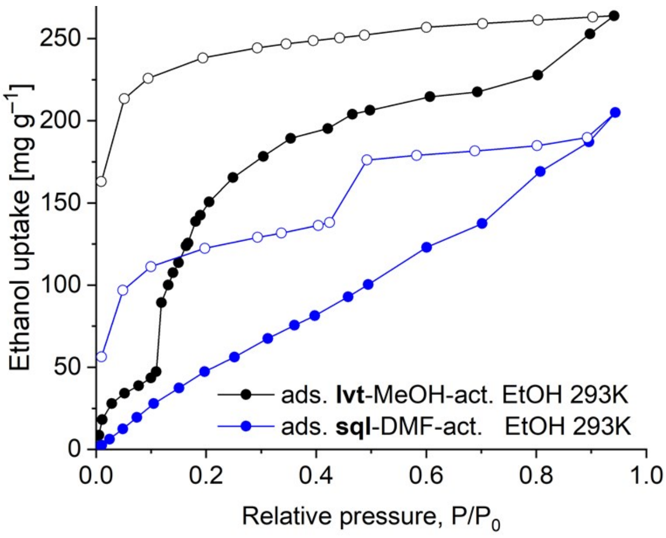

Fig. S21 Ethanol sorption of **lvt**-MeOH-act. and **sql**-DMF-act. at 293 K with the adsorption points as filled symbols and the desorption points as open symbols. Note that for **sql-**DMF the hysteresis loop contains a step at $P/P_0 \approx 0.45$ which hints at a framework flexibility.

References

1 Database NIST Chemistry WebBook; 25.06.2019; link https://webbook.nist.gov/chemistry/ accessed 13.24 h.
2 OriginPro, Version 2019, OriginLab Corporation, Northampton, MA, USA.
3 M. R. Bryant, A. D. Burrows, C. M. Fitchett, C. S. Hawes, S. O. Hunter, L. L. Keenan, D. J. Kelly, P. E. Kruger, M. F. Mahon and C. Richardson, *Dalton Trans.*, 2015, **44**, 9269–9280.
4 A. L. Spek, Structure Validation in Chemical Crystallography. *Acta Crystallogr. D*, 2009, **65**, 148–155; PLATON – A Multipurpose Crystallographic Tool, Utrecht University, Utrecht, The Netherlands, A. L. Spek, 2008; Windows implementation: L. J. Farrugia, University of Glasgow, Scotland, Version 280317, 2020.
5 X.-J. Yang, F. Drepper, B. Wu, W.-H. Sun, W. Haehnel and C. Janiak, *Dalton Trans.*, 2005, 256-267 and Supplementary

Material therein; C. Janiak, *J. Chem. Soc.*, *Dalton Trans.*, 2000, 3885-3896.

6 M. Nishio, *Phys. Chem. Chem. Phys.*, 2011, **13**, 13873-13900; M. Nishio, Y. Umezawa, K. Honda, S. Tsuboyama and H. Suezawa, *CrystEngComm*, 2009, **11**, 1757-1788; (d) M. Nishio, *CrystEngComm*, 2004, **6**, 130-158; C. Janiak, S. Temizdemir, S. Dechert, W. Deck, F. Girgsdies, J. Heinze, M. J. Kolm, T. G. Scharmann and O. M. Zipffel, *Eur. J. Inorg. Chem.*, 2000, 1229-1241; Y. Umezawa, S. Tsuboyama, K. Honda, J. Uzawa and M. Nishio, *Bull. Chem. Soc. Jpn.*, 1998, **71**, 1207-1213; M. Nishio, M. Hirota and Y. Umezawa, *The CH/π interaction (evidence, nature and consequences)*, Wiley-VCH, New York, 1998.

7 R. L. Sang and L. Xu, *CrystEngComm*, 2010, **12**, 1377-1381.

8 Mercury CSD 3.9, Program for Crystal Structure Visualisation, Exploration and Analysis from the CambridgeCrystallographic Data Center, Copyright CCDC 2001-2016, http://www.ccdc.cam.ac.uk/mercury/

9 F. Jeremias, A. Khutia, S. K. Henninger and C Janiak, *J. Mater. Chem.*, 2012, **22**, 10148–10151.

10 F. Jeremias, V. Lozan, S. K. Henninger and C. Janiak, *Dalton Trans.*, 2013, **42**, 15967–15973.